Periodic jetting and monodisperse jet drops from oblique gas injection

Oliver McRae, Antoine Gaillard, and James C. Bird

Phys. Rev. E **96**, 013112 — Published 19 July 2017

DOI: 10.1103/PhysRevE.96.013112

Periodic jetting and monodispere jet drops from oblique gas injection

Oliver McRae,[1] Antoine Gaillard,[1,2] and James C. Bird[1,*]

[1] *Department of Mechanical Engineering, Boston University, Boston, MA 02215, USA*

[2] *Department of Physics, Ecole Normale Superieure, 24 rue Lhomond 75005 Paris, France*

(Dated: June 28, 2017)

Abstract

When air is blown in a straw or tube near an air-liquid interface, typically one of two behaviors is observed: a dimple in the liquid's surface, or a frenzy of sputtering bubbles, waves, and spray. Here we report and characterize an intermediate regime that can develop when a confined air jet enters the interface at an angle. This regime is oscillatory with a distinct characteristic frequency and can develop periodic angled jets that can break up into monodisperse aerosols. The underlying mechanisms responsible for this highly periodic regime are not well understood. Here, we flow a continuous stream of gas through a tube near a liquid surface, observing both optically and acoustically the deformation of the liquid-air interface as various parameters are systematically adjusted. We show that the Kelvin-Helmholtz instability is responsible for the inception of waves within a cavity formed by the gas. Inertia, gravity, and capillary forces both shape the cavity and govern the frequency and amplitude of these gas-induced cavity waves. The flapping cavity focuses the waves into a series of periodic jets that can break up into droplets following the Rayleigh-Plateau instability. We present scaling arguments to rationalize the fundamental frequencies driving this system, as well as the conditions that bound the periodic regime. These frequencies and conditions compare well with our experimental results.

* jbird@bu.edu

I. INTRODUCTION

When a steady stream of gas passes through a tube near a stationary liquid interface, the interface typically exhibits one of two behaviors. If the orifice is relatively far away or if the flow rate is low enough, the liquid surface dimples [1, 2]. Alternatively, if the orifice is close to or below the liquid surface, or if the flow rate is relatively high, the surface erupts into a frenzy of waves, bubbles and droplets [1]. This bubbling can be random or regular, as is the case with air sparging [3]. Many previous studies have focused on the vertical impingement of gas jets above a liquid surface, resulting in the production of waves and polydisperse droplets [4, 5]. We explore a regime between these two expected behaviors for oblique impingement, a regime that is characterized by the formation of periodic jets formed by the flow of a gas through a nozzle angled near or below the liquid interface. Although this regime has been noted [6], to our knowledge it has not been systematically investigated.

The existence and boundaries of the periodic jetting regime explored in this article, as well as surrounding regimes, can be seen by flowing gas through a tube near to a liquid surface while varying the tube angle (figure 1). Here, nitrogen gas steadily flows through a tube resting on the bottom of a shallow Petri dish filled with 10 cSt silicon oil. At shallow angles, the liquid interface is deformed slightly by the flowing gas, creating a steady, stationary cavity (figure 1a). As the angle of inclination increases, it reaches a critical value θ_{wave}, above which the interface becomes unstable and waves propagate radially across the surface (figure 1b). As the angle increases further, the waves focus into a wide oscillating jet, or bulge, near the end of the tube outlet (figure 1c). This jet continues to focus with increasing angle and eventually becomes sufficiently long and narrow to pinch into monodisperse droplets that roll along the liquid interface (figure 1d). Indeed, if the jet is sufficiently long and narrow, more than one drop can pinch off as the jet recoils (figure 1e). Ultimately, the tube will reach another critical angle, θ_{bubble}, where periodicity gives way to an irregular eruption of bubbles, jets and droplets (figure 1f). This irregular regime appears qualitatively similar to the sputtering or splashing regime observed in asymmetric air jet impingement [1, 5, 7]. The phenomenon resembles the regimes created by gas jets vertically impinging on a liquid surface [4], and along with the presence of gas flowing across the fluid interface, draws parallels with typical atomisation [8, 9]. Unlike the monodisperse droplets observed in the current study, the droplet distribution from vertically impinging jets or typical atomisation

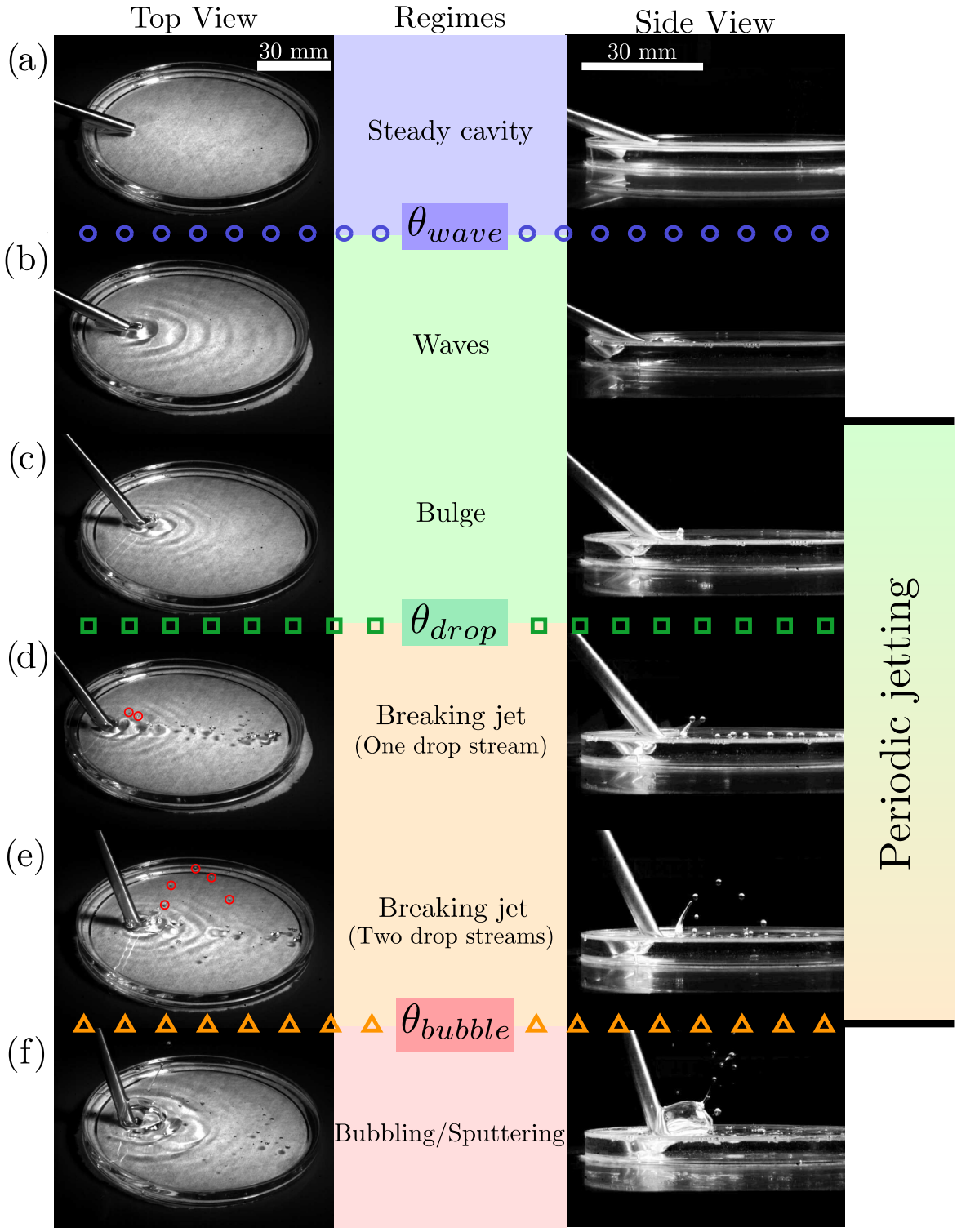

FIG. 1. Gas injection into a Petri dish of silicone oil can exhibit various dynamics. As the angle of the tube with the liquid surface is increased, there is a progression from a steady cavity to periodic waves, a stream of monodisperse droplets, and eventually a frenzy of bubbles and polydisperse droplets.

is irregular and polydisperse, indicating distinct mechanistic differences.

Although we are not aware of any previous studies detailing the regular oscillatory jets of liquid formed by air injection (figure 1c-e), aspects of the phenomenon resemble various known multiphase oscillators. The onset of waves is similar to the transition to large amplitude waves in stratified two-phase pipe flow, where the Kelvin-Helmholtz instability governs the transition [10]. The oscillations of liquid and gas at the end of the tube also bear similarities with the glug-glug of an inverted closed bottle, an instability linked to compressibility effects of the gas [11]. The formation of a stationary oscillatory jet is characteristic of the parametric excitation responsible for Faraday waves [12]. The oscillation frequency is similar to an observed turbulence-induced interface-instability [13], and the formation of a stream of equal-sized droplets resemble that formed by the Rayleigh-Plateau instability in flow-focusing microfluidic devices [14].

In the present study, we investigate the conditions necessary to create focused periodic perturbations on the deformed interface, a phenomenon that we refer to as cavity waves. We design a setup to systematically measure the characteristic frequency and present a map to depict the regime boundaries. We analyze the acoustic data to assess the periodicity of the regimes. Finally, we develop scaling arguments for the regime transitions and the underlying parameters responsible for the fundamental frequency in the particular region in which cavity waves focus to form oscillating jets.

A relevant feature of the oscillating jets documented in this study is their ability to break up into aerosol droplets. We expect the periodic jets to behave similarly to isolated finite liquid filaments, breaking up into one or more droplets based on the aspect ratio and liquid properties [15]. Aerosols are pertinent to a variety of industrial applications and natural global processes [16, 17]. Certain aerosol formation can be detrimental, such as those that vectorize and transport airborne pathogens through the pulmonary tract [18]. Aerosols of various sizes are generated from different sites within the airways, and the precise mechanisms leading to the formation of respiratory aerosols are still not well understood [19]. Indeed, of the four modalities of aerosol formation, three are related to airflow near an air liquid interface [20]. Thus, a better understanding of how a gas flow near an interface can generate aerosols may help to explain why and how some of these respiratory aerosols form. More generally, the dynamics arising from an impinging gas jet is of importance in certain industrial processes, such as arc welding [21] and steelmaking [7]. The transitions between

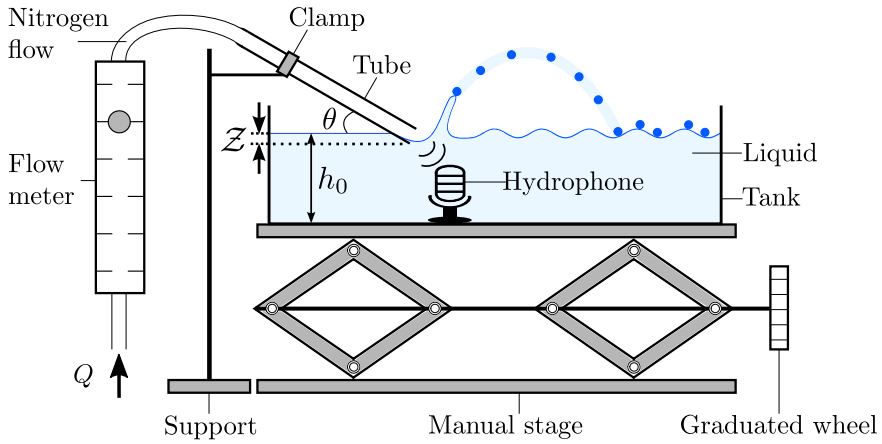

FIG. 2. A schematic of the experimental setup. The liquid is placed in a tank on a microstage to precisely control the distance $\mathcal{Z}$ that the tube is submerged. The tube angle θ and flow rate Q are also measured and varied.

different interfacial dynamics for inclined jets may be relevant to these processes.

II. METHODS

The experimental setup used to investigate the parameter space of the periodic jetting phenomenon is shown in figure 2. A liquid-filled tank sits atop a microstage, allowing this liquid bath to move vertically ($\pm$ 40 μm) relative to a circular tube used to inject gas across the liquid surface. This relative distance sets the depth $\mathcal{Z}$ of the bottom of the tube beneath the free surface. The angle of the tube can be adjusted independently of the bath, allowing for a variation in the angle θ between the horizontal and tube axes. The depth of the liquid in the bath $h_0 = 30$ mm is chosen to be deep enough to have a negligible influence on the interface dynamics. It should be noted that even with a much shallower liquid depth in the petri dish, (figure 1) the jetting phenomenon investigated is qualitatively similar. We have selected 10 cSt silicone oil as the bath liquid and nitrogen gas as the injected fluid. Elements of the phenomenon can be observed with water, but the full features are sharpened by using a slightly more viscous liquid with lower surface tension to attenuate shorter-wavelength capillary waves. These shorter waves are sensitive to experimental details affected by boundary conditions and confound interpretation of the underlying mechanisms that we investigate here. The viscosity μ and density ρ of each fluid are reported in Table I, along with the interfacial tension γ between these fluids, as reported by the manufacturer.

Fluid	μ (Pa s)	ρ (kg m^{-3})	γ (mN m^{-1})
Nitrogen (gas)	1.76×10^{-5}	1.16	
Silicone oil 10 cSt	9.35×10^{-3}	935	20.1

TABLE I. Viscosity, density, and surface tension of the two fluids used in the experiments.

The fixed, circular tube has an internal diameter of either $d = 4.8\,\text{mm}$ or $d = 6.2\,\text{mm}$ and is connected to a high pressure nitrogen tank via a regulation system that provides precise control over the flow rate Q. The flow rate can be adjusted with a precision of $\pm$ 4 mL/s.

Thus, the relevant geometrical properties of the system are the tube depth $\mathcal{Z}$, angle θ, and diameter d. The relevant physical properties are the densities ρ_1, ρ_2 and viscosities μ_1, μ_2 of the two fluids, where 1 refers to the liquid in the bath and 2 the gas flowing through the tube, surface tension γ and gravity g. The single dynamic property is the flow rate of the gas Q. The overall dynamics of the system are recorded with a combination of high-speed video using a Photron Fastcam SA5 high speed camera and high-resolution images with a Nikon D7000 DSLR. In addition, acoustic data is recorded using a hydrophone immersed in the liquid bath at the same initial horizontal distance from the tube outlet.

To assess the relative role of tube angle θ and depth $\mathcal{Z}$ on the interface dynamics, we sweep these two parameters and create a regime map. In the absence of flow ($Q = 0\,\text{mL/s}$), the tube is fixed at a particular angle θ and the bath raised until the inner edge of the tube outlet is at the same height as the liquid surface; this position defines the tube depth $\mathcal{Z} = 0$. Gas flow is introduced at a particular flow rate and fixed for the duration of a single sweep. The liquid bath is raised until a regime transition is detected from the high speed photography. The value of the tube depth $\mathcal{Z}$ at this height is recorded as a transition point. The bath continues to be raised – such that the subsequent transition points can be recorded in the same manner – until the random bubbling/sputtering regime is reached (see supplemental movie 1). The bath is then lowered and the transition points recorded a second time to confirm the absence of hysteresis in this system. The procedure is then repeated for different angles θ.

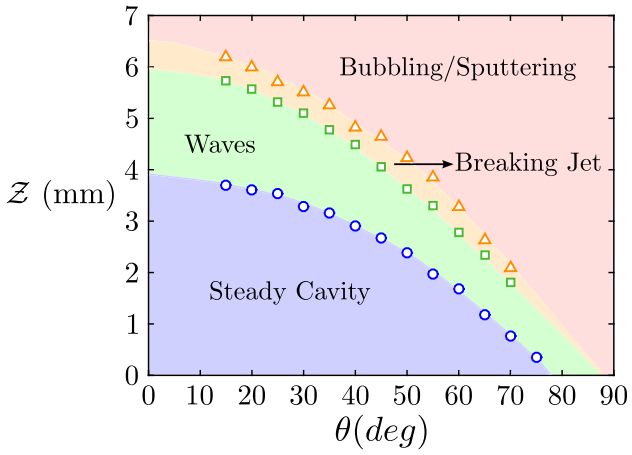

FIG. 3. An experimentally-derived regime map illustrates the interplay between tube submersion distance $\mathcal{Z}$ and inclination angle θ. Here the flow rate is $Q = 24$ mL/s, the internal diameter of the tube is $d = 4.8$ mm and all other parameters are fixed.

III. EXPERIMENTAL RESULTS

A regime map is portrayed in figure 3 with a flow rate $Q = 24\,\mathrm{mL/s}$, the internal diameter $d = 4.8$ mm and all other parameters fixed as described above. The lack of hysteresis and precision of the experimental setup lead to error bars smaller than the graphing markers used, as a result the error bars are not plotted. For a given angle θ, as the tube depth $\mathcal{Z}$ is increased, the interface transitions from a steady cavity to waves to breaking jets, and finally to a bubbling/sputtering regime. The same transition behavior, in terms of the order of regimes and lack of hysteresis, can be obtained by fixing the tube depth $\mathcal{Z}$, and increasing the angle θ, as indicated in figure 1.

A relation between the depth $\mathcal{Z}$ and angle θ becomes apparent when rescaling the data in figure 3 by $\mathcal{Z}/(d\cos\theta)$ (figure 4a). Below angles of approximately $\theta \approx 50°$, the transition points between the different regimes occur at constant values of $\mathcal{Z}/(d\cos\theta)$. This independence of the transition points for $\theta \lesssim 50$ also holds for the $d = 6.2$ mm tube. For these smaller values of θ, more of the air flows tangentially across the interface than normally impacts it. In contrast, at the higher values of θ, more of the flow impinges the liquid surface, and the dynamics may be more similarly to the impact of an impinging vertical air jet [1, 2].

Physically, the scaling $\mathcal{Z}/(d\cos\theta)$ can be interpreted as the ratio of the submerged depth $\ell = \mathcal{Z}/\cos\theta$ orthogonal to the tube relative to the tube diameter d (figure 4b). This ratio

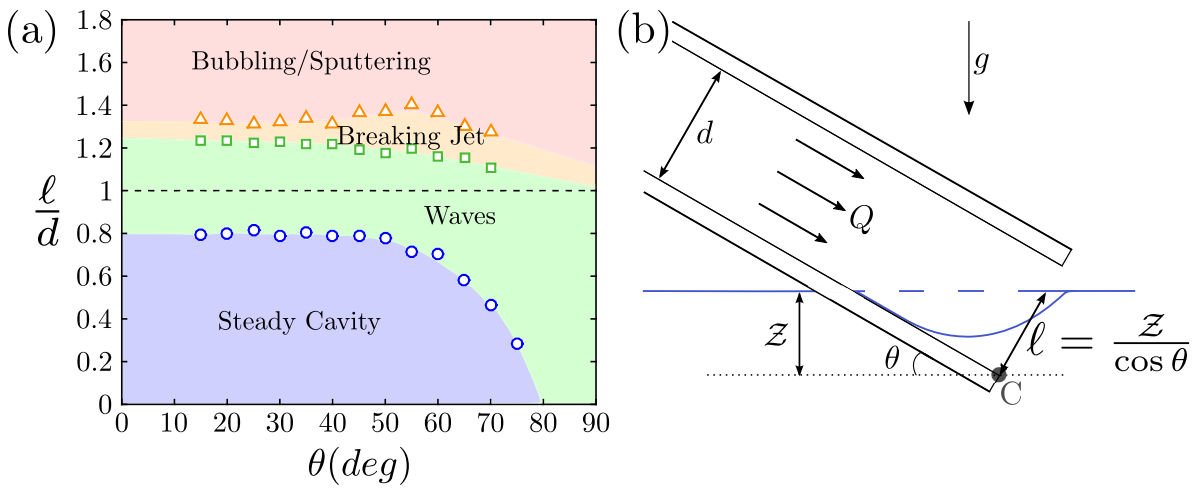

FIG. 4. Reducing dimensionality. (a) The regime map in figure 3 is non-dimensionalized and plotted in terms of $\mathcal{Z}/(d\cos\theta)$ and θ. At low angles, the regime boundaries occur at constant values of $\mathcal{Z}/(d\cos\theta)$ when all other parameters are fixed. Here the flow rate is $Q = 24$ mL/s, the internal diameter $d = 4.8$ mm. (b) The parameter $\mathcal{Z}/(d\cos\theta)$ can be geometrically interpreted as the fraction of the tube outlet that is submerged ℓ/d.

therefore represents an approximation for the fraction of the tube that is closed. Further parameter sweeps carried out in this paper are conducted at an angle $\theta = 30°$ and presented in terms of ℓ/d to take advantage of this reduction in dimensionality.

Note that we have selected the phases boundaries in figures 3 and 4 to correspond with abrupt changes in the interface dynamics. Specifically there is a sharp transition at the onset of waves (circles in figures 3 and 4), a topological change associated with the aerosol formation from the breaking jets (squares), and a sudden audible breakdown in periodicity associated with sputtering (triangles). The periodic jets identified in this article do not have a clear onset and instead develop smoothly from the waves interacting with a pronounced cavity (figure 1c). From experiments it appears that this onset occurs when $\ell/d \approx 1$ (see supplemental movie 1).

The acoustic signal of the flow can provide insight into the different regimes in Figure 4, especially as it relates to their regularity [22, 23]. In our setup, a hydrophone records a one-minute audio file for a given set of parameters. The mean spectrum is obtained by averaging over the Fourier transform of every 10 s of the audio file. Figure 5 presents the acoustic signature in both the spatial and frequency domains. When the cavity develops waves fig-

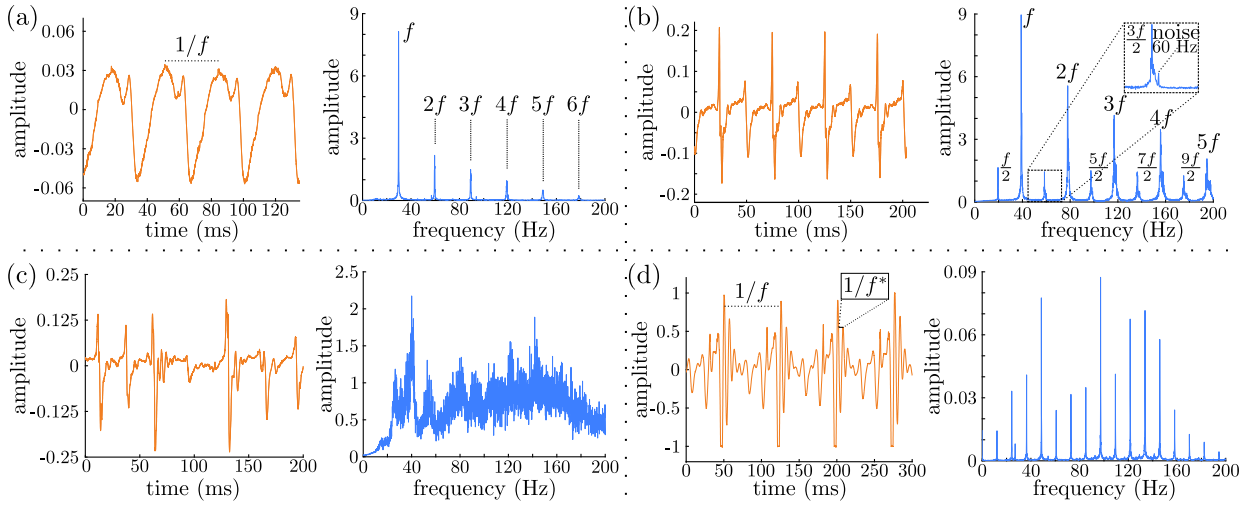

FIG. 5. Acoustic signatures captured by the hydrophone for the various dynamic regimes: (a) wave regime [$\ell/d = 1.0$, $Q = 47$ mL/s], (b) breaking jet regime [$\ell/d = 1.4$, $Q = 47$ mL/s], and (c) irregular bubbling/sputtering regime [$\ell/d = 1.4$, $Q = 16$ mL/s]. (d) A distinctly different acoustic signature appears for the bubbling regime at a low enough flow rate that a periodic stream of bubbles rise to the liquid surface and rupture [$\ell/d = 1.4$, $Q = 8$ mL/s]. Each set of acoustic data is plotted in both the spatial domain (left) and the frequency domain (right). Here $d = 30$ mm and $\theta = 30°$.

ure 5a, the hydrophone measures pressure fluctuations that correspond to these interfacial waves. Indeed, highspeed imaging confirms that the fundamental frequency from the acoustics matches with the frequency of the air-liquid interface displacement. The breaking jet regime exhibits a more complex acoustic signature, rich in harmonics and subharmonics (figure 5b). Note that there is a slight shift in the fundamental frequency between these two regimes; however both frequencies are in the range of 30 to 40 Hz. The electronic noise at 60 Hz is also visible in the spectrum, but has a negligible contribution. In the bubbling/sputtering regime, the acoustics are far more complex and lack a clear fundamental frequency, providing evidence for the chaotic nature of this regime (figure 5c). The spectrum of the bubbling regime changes when the flow rate is significantly reduced, forming a range of distinct frequencies (figure 5d). Here a single bubble stream is emitted from the completely submerged tube and the detected sound is likely due to both the collapse of the air connection at bubble detachment [24] and by the rupturing bubble at the surface [25].

It is natural to inquire whether a change in flow rate affects other boundaries and fre-

quencies. To address this question, we complete another parameter sweep in which the flow rate Q and depth $\mathcal{Z}$ are varied, while maintaining a fixed tube angle $\theta = 30°$. The regime map and the accompanying fundamental frequency for each flow rate are shown in figure 6. The fraction ℓ/d at which the tube needs to be submerged to generate waves decreases with increased flow rate of gas Q (circles in figure 6a). When the tube is fully submerged ($\ell/d > 1$), the system can create periodic jets or bubbling/sputtering. Here it appears that the transition to jet break-up and bubbling are nearly independent of the flow rate. At low flow rates, the bubbling is periodic, (denoted by the asterisk in figure 6a) however the transition to this regime of periodic bubbling was not systematically investigated. Repeating these experiments for a larger tube ($d = 6.2\,\text{mm}$), we find the dynamics follow the same trend. The fraction ℓ/d at which the tube needs to be submerged to generate waves decreases with increased flow rate of gas. Similarly when the larger tube is fully submerged ($\ell/d > 1$), the system also can create periodic jets or bubbling/sputtering with transition for periodic jets occurring around $\ell/d = 1$ and bubble/sputtering at values between 1.2 and 1.3 that also appear independent of flow rate and θ.

Between the steady cavity and bubbling/sputtering regimes, there is a clear fundamental frequency f obtained from the acoustics (figure 6b). For the $d = 4.8$ mm tube (open symbols in figure 6b), this frequency ranges from approximately 20 to 40 Hz. As the tube outlet fraction ℓ/d increases, the frequency f increases. The dependence of frequency on the flow rate Q is less pronounced and appear to be non-monotonic, first decreasing and then increasing with increasing flow rate. Of particular interest is the frequency when $\ell/d \gtrsim 1$ (darker symbols in figure 6b), as this condition is linked to the periodic jetting regime. When hydrophone experiments are repeated for the larger tube ($d = 6.2\,\text{mm}$) for these tube outlet fractions ℓ/d, a slightly lower fundamental frequency f is observed (closed symbols in figure 6b).

IV. MODELING AND DISCUSSION

A. Onset of Periodicity

The periodic jetting regime documented in this article is bounded on one side by the onset of waves and on the other by the formation of bubbles and sputters. Focusing first on the

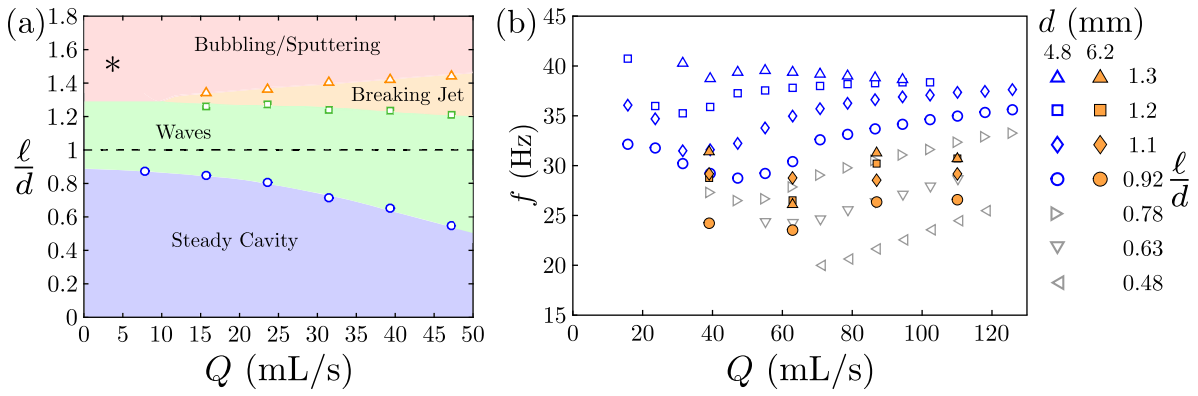

FIG. 6. Experimental data illustrating the role of flow rate Q. (a) The regime map as a function of tube outlet fraction ℓ/d and flow rate Q with $d = 4.8$ mm. (b) The fundamental frequencies f in the periodic regime (waves and breaking jet) as a function of flow rate Q and tube outlet fraction ℓ/d. Conditions with $\ell/d \gtrsim 1$ are repeated with a larger diameter $d = 6.2$ mm tube. Here the tube angle is fixed at $\theta = 30°$. The $*$ region represents the regime of regular bubbling observed at high tube submersion and low flow rates. The transition from the regular/periodic bubbling regime to irregular bubbling was not systematically investigated.

transition from the steady cavity to the formation of waves, our data shows that the tube is never fully submerged ($\ell/d < 1$) when this transition takes place (figure 7b). Furthermore, the amount of tube submersion at the onset of waves decreases with increasing flow rate Q. This trend is consistent with a shear-induced instability. Indeed, we can develop a falsifiable model to test the hypothesis that the onset of waves is due to a Kelvin-Helmholtz instability, rather than other instabilities such as those responsible for the glug-glug in bottles [11].

The Kelvin-Helmholtz instability occurs when there is a velocity difference at the interface between two fluids [26, 27]. If the velocity difference at the interface $\Delta U = |U_2 - U_1|$ is greater than a critical value, the shear stress will overcome the restoring forces of surface tension and gravity, amplifying small perturbations of the interface into waves. For an initially flat interface between two inviscid fluids the threshold velocity is given by

$$U_c = \left(2\frac{\rho_1 + \rho_2}{\rho_1 \rho_2} \sqrt{(\rho_1 - \rho_2)\, g\gamma} \right)^{1/2}. \tag{1}$$

To estimate the instability criterion for the system described in this paper, we relate U_2 to the velocity of the gas at the tube outlet and U_1 to the velocity of the liquid at the interface. We assume that this interface velocity U_1 is nearly stationary. Indeed, we directly

measure the liquid velocity U_1 to be consistently 2 orders of magnitude lower than the gas velocity U_2. These measurements are obtained by seeding the liquid with micrometric sized bubbles and tracking the bubble motion near the interface.

For incompressible flow in a confined tube, the relationship between the flow rate Q and the average gas velocity at the tube outlet is given by $U_2 = \frac{Q}{A_e}$, where A_e is the cross-sectional area of the exiting gas (figure 7a). This area is related geometrically to ℓ/d by

$$A_e = \frac{d^2}{8}\zeta\left(\ell/d\right) \qquad \text{with} \qquad \zeta\left(x\right) = 2\arccos(2x-1) - \sin(2\arccos(2x-1)). \tag{2}$$

Therefore the average velocity of the gas is given by

$$U_2 = Q \Big/ \left[\frac{d^2}{8}\left\{2\arccos\left(2\frac{\ell}{d}-1\right) - \sin\left[2\arccos\left(2\frac{\ell}{d}-1\right)\right]\right\}\right]. \tag{3}$$

If the transition from the steady cavity to the wave regime is due to a Kelvin-Helmholtz instability, then we would expect the transition to occur when the gas velocity U_2 is approximately equal to the instability onset velocity U_c. With a large density difference between the two fluids, as is the case in this study, equation 1 can be simplified, so that the transition between the regimes would occur when $U_2 = \sqrt{2\frac{(\rho_1 g\gamma)^{1/2}}{\rho_2}}$. Therefore, the predicted transition can be expressed in terms of the flow rate Q and tube submersion distance ℓ as

$$\frac{\ell}{d} = \zeta^{-1}\left[4\sqrt{2}\left(\frac{Q}{d^2}\right)\sqrt{\frac{\rho_2}{(\rho_1 g\gamma)^{1/2}}}\right] \approx 1 - \left(\frac{2\sqrt{2}}{\pi}\right)\left(\frac{Q}{d^2}\right)\sqrt{\frac{\rho_2}{(\rho_1 g\gamma)^{1/2}}}. \tag{4}$$

These expressions, both exact and the approximate, are plotted in figure 7b. The approximation can be physically interpreted as the depth at which the transition to waves would occur in an equivalent square tube. Alongside these theoretical predictions are the experimental results from figure 6a, nondimensionalized and extended to include even higher flow rates, as well as additional data taken with the larger diameter tube. With a greater immersion depth ℓ/d, and thus smaller gas exit area A_e, the flow rate required to induce a transition to the wave regime is lowered. When the flow rate is scaled following equation 4, the experimental data for the onset of waves collapse onto a master curve that is consistent with our model (figure 7b). Therefore our data suggests that the onset of waves for the partially submerged tube is indeed due to the Kelvin-Helmholtz instability.

Note that the model slightly underestimates the experimental data, likely attributable to the model's assumption of a flat static interface and a sharp velocity discontinuity in the

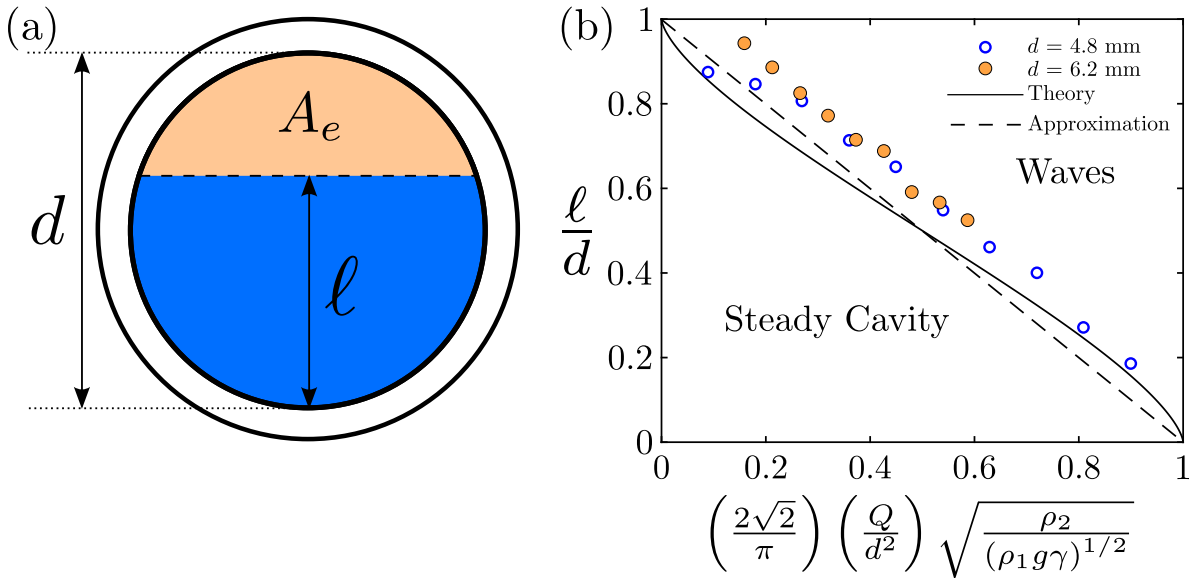

FIG. 7. Transition for steady cavity to waves. (a) A schematic of the area of the tube outlet fraction available for the flow of gas. (b) Experimentally measured transition values for two different diameter tubes are plotted for various tube outlet fractions and non-dimensional flow rates and compared to theory.

flow profile at the interface. The angle of the tube is included in the analysis through its effect on the cross-sectional area A_e and the length $\ell = \mathcal{Z}/\cos\theta$. However, as noted in the schematic figure 4b, the flowing gas is also angled and exerts a deforming force on liquid surface. This force is balanced by gravity and capillary forces acting to flatten the interface, which gives rise to the steady cavity similar to that previously described for perpendicular gas flow [1, 2]. As the gas flow rate is increased, the liquid level at the tube outlet decreases below ℓ due to the cavity (figure 4b). This lowering of the liquid level effectively increases the gas exit area A_e and requires a higher flow rate Q to achieve the critical velocity U_c and may explain the rightward shift of the experimental data from the theoretical curve in figure 7b. The model also assumes gas flow tangent to the liquid interface, based on our experimental results on the independence of the transition points ℓ/d with $\theta \lesssim 50$, we expect the model to be valid over this range of angles θ as well. A correction factor is not implemented in the model as the assumption of an initially flat interface is sufficient to capture the underlying relationship between the transition points, flow rate and the immersion depth, albeit offset from the experimental data. Based on the similarity between the model and experiments, corrections also do not seem to be necessary to account for a continuous velocity profile,

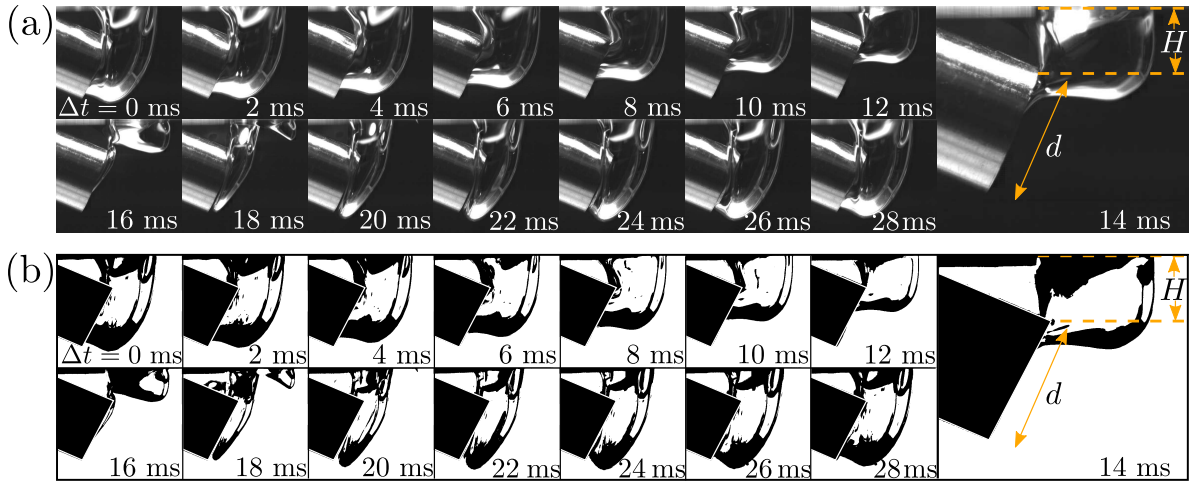

FIG. 8. (a) A time series of high-speed images representing one period of the breaking jet regime. Here the tube is fully submerged a distance H from the free surface. (b) The high-speed images from (a) thresholded with the tube masked to provide better visualization of the interface.

even though it is known that the Kelvin-Helmholtz instability is often sensitive to the precise shape of the gas boundary-layer [27, 28].

B. Breakdown of Periodicity

The transition from a steady cavity to the wave regime marks the onset of periodicity in the system. With the continued lowering of the tube, the waves form on a well-defined cavity and focus to form periodic jets. Much of this periodic jetting, including the breaking jets, occur when tube is fully submerged below the interface ($\ell/d > 1$). Yet in these cases, there appears to be a connected path for the gas to flow from the tube to the atmosphere (figure 8). However, for sufficiently large values of ℓ/d, this pathway can pinch apart each period, severing the connection to the surface and creating distinct bubbles. For flow rates higher than in the periodic bubbling regime (marked by $*$ in figure 6a), the collapse of these bubbles at the surface produces a cacophony of waves, jets and droplets, which may be best described as sputtering (figures 5c). For values of $\ell/d > 1$, we are able to introduce a new dimension $H = \mathcal{Z} - d\cos\theta$; H represents the vertical distance between the top of the tube outlet and the unperturbed bath liquid surface (figure 8).

Pinch-off at the tube outlet occurs when buoyancy forces overcome capillary forces [29], which translates roughly to a detaching bubble diameter that is larger than the capillary

length $\lambda_c = \sqrt{\frac{\gamma}{\rho_1 g}}$. Provided that the tube is submerged at a depth below this critical detaching bubble diameter ($H > \lambda_c$), a bubble can detach from the tube, separating the gas within the tube from the surrounding atmosphere. Conversely, provided that $H < \lambda_c$, there remains a conduit for the gas between the tube and the atmosphere. If cavity pinch-off indeed is responsible for the transition into the bubbling/sputtering regime, then the transition would be expected to occur at a critical tube depth $\mathcal{Z} \approx d\cos\theta + \lambda_c$, or equivalently

$$\frac{\ell_{bubble}}{d} \approx 1 + \frac{\lambda_c}{d\cos\theta}. \tag{5}$$

Note that this transition is independent of flow rate Q and instead depends on the properties of the liquid λ_c, the diameter of the tube d, and θ. This prediction is quantitatively consistent with the experimentally observed transitions shown in figure 6a. For these parameters—$\lambda_c = 1.48$ mm, $d = 4.8\,$mm, $\theta = 30°$—the bubbling/sputtering transition is predicted to occur when $\ell/d \approx 1.36$. With the larger tube at this angle, the transition is predicted to be slightly lower, which is consistent with our observations. These comparisons illustrate that the model captures the effects of flow rate and tube diameter; however, equation 5 also predicts a dependence on inclination angle θ, which interestingly is not readily apparent in the experimental data shown in figure 4. For angles $\theta < 50°$, $\frac{\ell_{bubble}}{d}$ is predicted to range from approximately 1.31 to 1.48 for the $d = 4.8\,$mm tube. Yet for higher inclination angles, the predicted transition rapidly diverges from the experimental data, suggesting that the model is only appropriate for lower inclination angles.

C. Modeling the Fundamental Frequency

With both transitions theoretically defined, we now have a lower and upper bound for the region of periodicity and can look within the region itself. Our acoustic results indicate that there is a fundamental frequency f in the periodic regime that increases with increasing tube depth ℓ and decreases with increasing tube diameter d (figure 6). Here we have focused on changing the dimension orthogonal to the tube tip ℓ and recorded the effect this change has on regime transition and frequency. However, specific emphasis must be made of the three dimensional nature of this phenomenon, especially as it relates to the focusing effect of the collapsing cavity. The formation of jets from collapsing cavities has long been appreciated in the oceanography community [30, 31] and has recently also been shown to occur when

cavities are created by single pulsed air jets [32].

At a right azimuthal angle to ℓ, the tube diameter d plays an important role in setting the collapse dynamics of the cavity. The collapsing cavity waves not only have to traverse the vertical distance ℓ but also a spanwise distance set by the tube diameter d. For $\ell/d < 1$ there is an increase in the frequency with increasing ℓ which may be due to an increased restoring force from the increased cavity curvature (figure 6b). For $\ell/d \gtrsim 1$ there is a limitation, the distance d, in the vertical distance the waves can travel due to the tube confinement. With comparable length scales in the vertical and spanwise directions, a focusing effect can be seen as the waves meet during the collapse of the cavity, creating the periodic jetting seen in figure 1c-e. Also, the effect of ℓ on the frequency is significantly diminished, reinforcing the use of d as the dominant length scale in the periodic jetting regime (figure 6b).

Inspection of figure 8 reveals that when the tube is submerged ($\ell/d \geq 1$), there is a convective time associated with the liquid-gas interface rising and constricting the gas flow out the end of tube. Indeed, once the liquid nearly constricts the tube opening ($\Delta t = 14\,\mathrm{ms}$ in figure 8) this liquid is rapidly cleared. Therefore the time τ for a wave traveling with speed c to constrict a tube with diameter d can be related to the fundamental frequency f as

$$\tau = \frac{d}{c} = \frac{1}{f}. \tag{6}$$

The waves formed by the collapsing flapping cavity follow the dispersion equation for waves under the influence of gravity and capillarity at the interface of fluids of infinite depth ($h_0 \gg \frac{1}{2}\lambda$),

$$\omega = \sqrt{gk + \frac{\gamma k^3}{\rho_1}} \tag{7}$$

where ω is the angular frequency and k the wavenumber [33]. These waves propagate with a phase velocity v_p given by

$$v_p = \frac{\omega}{k} = \sqrt{\frac{g}{k} + \frac{\gamma k}{\rho_1}}. \tag{8}$$

The cavity waves propagate naturally at the minimum of the phase velocity, when there is a balance between gravitational and capillary effects. This minimum occurs when the wavelength is the capillary length of the bath liquid, λ_c. This wavelength results in a critical wavenumber

$$k_c = \frac{1}{\lambda_c} = \sqrt{\frac{\rho_1 g}{\gamma}}, \tag{9}$$

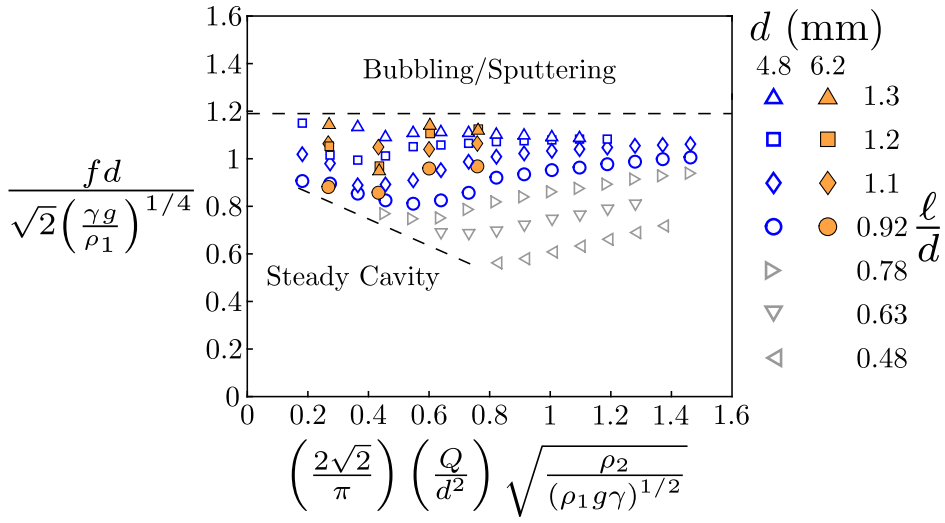

FIG. 9. The frequency response (figure 6b) for two different diameter tubes plotted using the dimensionless frequency and the dimensionless flow rate suggested from the proposed mechanism. The broken lines are visual aids bounding the region of periodicity.

which when used in equation 8 gives the wavespeed

$$c = \sqrt{g\left(\frac{\gamma}{\rho_1 g}\right)^{1/2} + \frac{\gamma}{\rho_1}\left(\frac{\rho_1 g}{\gamma}\right)^{1/2}} = \sqrt{2}\left(\frac{\gamma g}{\rho_1}\right)^{1/4}. \tag{10}$$

Equations 6 and 10 can be combined and rearranged to reveal that

$$\frac{fd}{\sqrt{2}\left(\frac{\gamma g}{\rho_1}\right)^{1/4}} = 1. \tag{11}$$

This combination of parameters can be interpreted as a non-dimensional frequency, or alternatively as a Strouhal number, and can be used to predict the fundamental frequency based on the material and geometric parameters.

To test this prediction, we re-plot the experimental data presented in figure 6b on axes that correspond to our proposed non-dimensional flow rate and non-dimensional frequency (figure 9). Data points are bound by the steady cavity and bubble regimes. For values of $\ell/d \gtrsim 1$ (the darker symbols in figures 6b and 9), values on which our model is based, the non-dimensional frequency is indeed approximately one, revealing that our experimental results are consistent with our model predictions. Equally important, the experimental data for the two different diameter tubes collapse, supporting the frequency scaling and its dependence on the tube diameter d.

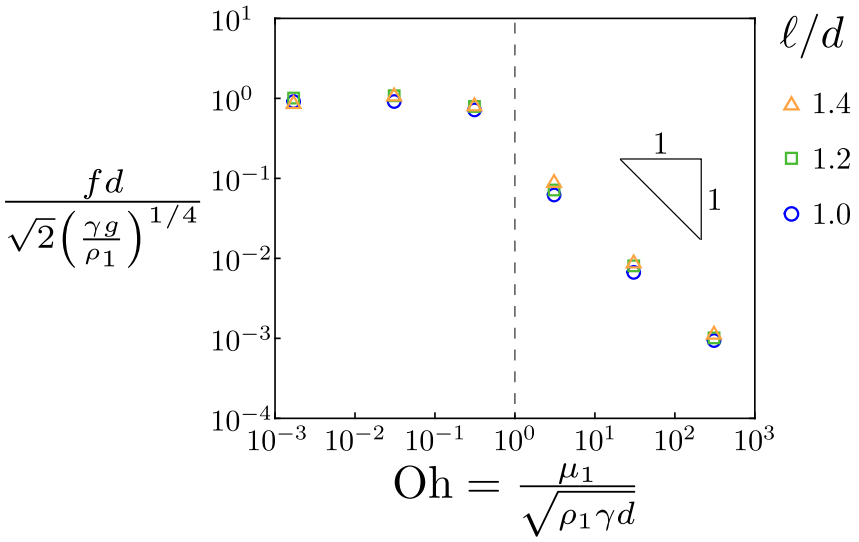

FIG. 10. Effect of viscosity on frequency response. The dimensionless frequency is plotted against an Ohnesorge number and indicates the relative contribution of viscosity to the dynamics of the phenomenon. The fluids used, in order of increasing viscosity, are water and silicone oils of viscosity 10, 100, 1000, 10,000 and 100,000 cSt.

Note that all of the dimensionless groups are independent of viscosity. Viscous effects can be quantified through the Ohnesorge number $\mathrm{Oh} \equiv \frac{\mu_1}{\sqrt{\rho_1 \gamma d}}$, which indicates the balance between viscous, inertial and surface tension forces. For the results presented, $\mathrm{Oh} = 0.03$; because this value is much less than one, the dynamics are likely dominated by inertial and surface tension forces. This balance reinforces the use of the inviscid Kelvin-Helmholtz theory [34] and suggests that the fundamental frequency should be independent of liquid viscosity provided that $\mathrm{Oh} \ll 1$. To test this prediction, we measure the fundamental frequency f at three different tube depths in different viscosity silicone oils. Figure 10 gives the dimensionless frequency plotted against the Ohnesorge number. For $\mathrm{Oh} \ll 1$ the dimensionless frequency is shown to be independent of the Ohnesorge number, and by extension viscosity. For an $\mathrm{Oh} \geq 1$ there is a transition to a viscous timescale with the dimensionless frequency scaling with Oh^{-1}. The results shown in figure 10 further support the use of the inviscid Kelvin-Helmholtz theory provided that the $Oh < 0.3$. The use of inviscid Kelvin-Helmholtz theory for the bath viscosity used in this study is further supported by previous work [35], which showed the independence of wave frequency and wavelength below a critical viscosity on the same order of magnitude shown in figure 10.

V. CONCLUSION

In this paper, we systematically investigate the phenomena arising from steady gas injection through an angled tube at a gas-liquid interface. In particular, we explore a novel regime in which the stream of gas creates a periodically collapsing cavity in the liquid. This flapping cavity gives rise to an oscillating jet from which monodisperse droplets can be produced through the Rayleigh-Plateau instability. Through a combination of experiments and scaling arguments, we provide evidence that waves, driven by a Kelvin-Helmholtz instability focus into jets through the periodic collapse of the gas cavity. This periodic jetting regime is bounded on one side by the onset of the Kelvin-Helmholtz instability and the existence of a pronounced cavity ($\ell/d \approx 1$) and on the other side by the pinch-off of a conduit that permits gas to travel continuously from the injection tube to the atmosphere. Within these bounds, the system oscillates with a fundamental frequency that appears to be set by the cavity collapse speed and the tube diameter.

The gas-induced cavity waves bear the hallmarks of both a shear induced instability and jet-drop formation from a collapsing bubble. The combination of these two normally disparate topics in fluid mechanics may help experimentalists and theorists unlock a new class of liquid-gas oscillators capable of producing highly repeatable events, such as monodisperse droplets. Although our experiments are restricted to a liquid-gas system, the high frequency jet drop production may extend to analogous liquid-liquid systems and provide an efficient means to create monodisperse emulsions. Similarly, the tube-bath setup in this study shares geometric features with multiphase branched-tube networks, and our scaling results may provide insight into the creation of certain respiratory aerosols.

VI. ACKNOWLEDGEMENTS

We acknowledge Prof. Howard Stone for his help in laying the foundation of this work and to Dr. Yonas Gizaw for encouraging this study. We thank Dr. Casey Bartlett and Dr. Peter Walls for assistance with the experimental setup. We acknowledge the support of the École Normale Supérieure internship program and partial support from the National

Science Foundation under Grant No. 1351466.

[1] R. B. Banks and D. Chandrasekhara, J. Fluid Mech. **15**, 13 (1963).

[2] A. He and A. Belmonte, Phys. Fluids **22**, 042103 (2010).

[3] E. K. Nyer and S. S. Suthersan, Ground Water Monit. R. **13**, 87 (1993).

[4] R. Rosler and G. Stewart, J. Fluid Mech. **31**, 163 (1968).

[5] H. Y. Hwang and G. A. Irons, Metall. Mater. Trans. B **43**, 302 (2012).

[6] J. C. Bird and H. A. Stone, "Liquid acrobatics," (2008), arXiv:0810.1601.

[7] Subagyo, G. A. Brooks, K. S. Coley, and G. A. Irons, ISIJ Int. **43**, 983 (2003).

[8] T. Driessen, R. Jeurissen, H. Wijshoff, F. Toschi, and D. Lohse, Phys. Fluids **25**, 062109 (2013).

[9] B. M. Devassy, C. Habchi, and E. Daniel, Atomization Spray **25**, 47 (2015).

[10] C. Tzotzi and N. Andritsos, Int. J. Multiph. Flow **54**, 43 (2013).

[11] C. Clanet and G. Searby, J. Fluid Mech. **510**, 145 (2004).

[12] J. Miles, J. Fluid Mech. **248**, 671 (1993).

[13] J.-P. Matas, S. Marty, M. S. Dem, and A. Cartellier, Phys. Rev. Lett. **115**, 074501 (2015).

[14] S. L. Anna, N. Bontoux, and H. A. Stone, Appl. Phys. Lett. **82**, 364 (2003).

[15] A. A. Castrejón-Pita, J. Castrejon-Pita, and I. Hutchings, Phys. Rev. Lett. **108**, 074506 (2012).

[16] T. M. N. Nguyen, D. Ilef, S. Jarraud, L. Rouil, C. Campese, D. Che, S. Haeghebaert, F. Ganiayre, F. Marcel, J. Etienne, and J.-C. Desenclos, J. Infect. Dis. **193**, 102 (2006).

[17] J. Kim, Int. J. Heat Fluid Fl. **28**, 753 (2007).

[18] R. Tellier, J. R. Soc. Interface , rsif20090302 (2009).

[19] J. Gralton, E. Tovey, M.-L. McLaws, and W. D. Rawlinson, J. Infect. **62**, 1 (2011).

[20] L. Morawska, G. Johnson, Z. Ristovski, M. Hargreaves, K. Mengersen, S. Corbett, C. Chao, Y. Li, and D. Katoshevski, J. Aerosol Sci. **40**, 256 (2009).

[21] J. Berghmans, J. Phys. D **5**, 1096 (1972).

[22] M. Ruzicka, J. Drahoš, J. Zahradník, and N. Thomas, Int. J. Multiph. Flow **23**, 671 (1997).

[23] T. L. Szabo, J. Acoust. Soc. Am. **97**, 14 (1995).

[24] H. Czerski and G. B. Deane, J. Acoust. Soc. Am. **128**, 2625 (2010).

[25] D. E. Spiel, J. Geophys. Res. **97**, 11443 (1992).

[26] P. Drazin, *Introduction to Hydrodynamic Stability*, Cambridge Texts in Applied Mathematics (Cambridge University Press, 2002).

[27] J. Eggers and E. Villermaux, Rep. Prog. Phys. **71**, 036601 (2008).

[28] J. Gordillo, M. Pérez-Saborid, and A. Gañán-Calvo, J. Fluid Mech. **448**, 23 (2001).

[29] W. Fritz, Phvs. Z. **36**, 379 (1935).

[30] C. Kientzler, A. B. Arons, D. C. Blanchard, and A. H. Woodcock, Tellus **6**, 1 (1954).

[31] F. MacIntyre, J. Geophys. Res. **77**, 5211 (1972).

[32] É. Ghabache, T. Séon, and A. Antkowiak, J. Fluid Mech. **761**, 206 (2014).

[33] M. J. Lighthill, *Waves in fluids* (Cambridge University Press, Cambridge England New York, 1978).

[34] D. Barnea and Y. Taitel, Int. J. Multiph. Flow **19**, 639 (1993).

[35] A. Paquier, F. Moisy, and M. Rabaud, Phys. Rev. Fluids **1**, 083901 (2016).